

## Simulation of Power-Law Fluid Flows in Two-Dimensional Square Cavity Using Multi-Relaxation-Time Lattice Boltzmann Method

Qiuxiang Li<sup>1</sup>, Ning Hong<sup>2</sup>, Baochang Shi<sup>3\*</sup> and Zhenhua Chai<sup>3</sup>

<sup>1</sup> State Key Laboratory of Coal Combustion, Huazhong University of Science and Technology, Wuhan, 430074, P.R. China.

<sup>2</sup> Department of Foundational Courses, Jiangcheng College, China University of Geosciences, Wuhan, 430200, P.R. China.

<sup>3</sup> School of Mathematics and Statistics, Huazhong University of Science and Technology, Wuhan, 430074, P.R. China.

Received 16 February 2012; Accepted (in revised version) 21 May 2013

Communicated by Kazuo Aoki

Available online 16 August 2013

---

**Abstract.** In this paper, the power-law fluid flows in a two-dimensional square cavity are investigated in detail with multi-relaxation-time lattice Boltzmann method (MRT-LBM). The influence of the Reynolds number ( $Re$ ) and the power-law index ( $n$ ) on the vortex strength, vortex position and velocity distribution are extensively studied. In our numerical simulations,  $Re$  is varied from 100 to 10000, and  $n$  is ranged from 0.25 to 1.75, covering both cases of shear-thinning and shear-thickening. Compared with the Newtonian fluid, numerical results show that the flow structure and number of vortex of power-law fluid are not only dependent on the Reynolds number, but also related to power-law index.

**AMS subject classifications:** 76A05, 76M28, 76D05, 81T80

**Key words:** Multi-relaxation-time lattice Boltzmann method, power-law fluid, shear-thinning, shear-thickening.

---

## 1 Introduction

The non-Newtonian fluids are widely observed in many fields of science and technology, such as food, petroleum, lubricants, geophysics, hydrogeology, chemistry, to name but a

---

\*Corresponding author. *Email addresses:* sbchust@126.com (B. Shi), 11qqxxx@126.com (Q. Li), hn\_jxycy@126.com (N. Hong), hustczh@126.com (Z. Chai)

few. Moreover, many modern materials and manufacturing processes also require further understanding on the behavior of non-Newtonian fluids since their wide applications in practice [1,2]. Compared to the Newtonian fluids, the non-Newtonian fluids usually have a complicated constitutive equation, which may bring more difficulties in investigating non-Newtonian behavior with numerical methods. In the past years, some advanced or efficient methods have been developed to simulate the non-Newtonian fluid flows, such as finite element method [3], finite volume method [4], lattice Boltzmann method (LBM) [5] and smoothed particle hydrodynamics method (SPH) [6]. With the aid of the methods mentioned above, some complex flow features that differ from the Newtonian fluids have been reported.

In this paper, we will use a lattice Boltzmann method to study the behaviors of power-law non-Newtonian fluid flows in a two-dimensional square cavity. During the last two decades, the LBM, as a new mesoscopic method, has been proved to be a powerful numerical technique in simulating complex Newtonian and non-Newtonian fluid flows [7–9] and particularly successful in dealing with complex boundaries for its kinetic background [9–14]. Compared to some traditional numerical methods, another advantage of the LBM is that the stress tensor can be obtained locally from the non-equilibrium parts of the distribution functions [12,13]. Hence, the LBM is considered to offer excellent possibilities for simulating non-Newtonian flows [13].

A popular lattice Boltzmann model is the so-called lattice Bhatnagar-Gross-Kook model (LBGK) [14, 15], which has been widely applied to study complex flows. However, LBGK model is usually unstable when the relaxation time is close to 0.5. One way to overcome this shortcoming of the LBGK model is to use a multiple-relaxation-time (MRT) model, or generalized lattice Boltzmann model, which was originally proposed by d’Humières [16] and further developed by Lallemand and Luo [17]. Compared with the LBGK model, MRT model can improve the numerical stability and reduce the unphysical oscillations for some flows.

The lid-driven flow in a two-dimensional (2D) square cavity, as a classic benchmark problem in fluid mechanics, has been widely studied by many researchers [18–26] in the past decades. Driven cavity flow is of great importance because it can offer an ideal framework in which meaningful and detailed comparisons can be made between results obtained from theory and computation [20]. Besides, this problem has a simple geometry, but covers a wide range of complex hydrodynamics encompassing eddies, secondary flows, instability and transition, which are of great importance to the basic study of fluid mechanics. However, to the best of the knowledge of the authors, most available works are limited to the Newtonian fluids and only few works associated with the non-Newtonian (power-law) fluid flows in a square cavity have been reported. To fill the gap, in the present work, the LBM coupling with MRT model is used to simulate power-law non-Newtonian fluid flows in a two-dimensional square cavity (see Fig. 1). We intend to explore the complex phenomena of non-Newtonian fluid flows and investigate non-Newtonian effects in the lid-driven cavity flows, a detailed comparison of the non-Newtonian results with Newtonian results have been done.

The rest of the paper is organized as follows. In Section 2, we briefly review the model of power-law fluid flows. In Section 3, the LBM with MRT model is introduced. In Section 4, numerical results on the power-law fluid flows in a lid-driven cavity are presented and discussed. Finally, some conclusions are given in Section 5.

## 2 The model of the power-law fluid flows

The macroscopic continuous and momentum equations for two-dimensional flow of a generalized Newtonian fluid are given by

$$\frac{\partial \rho}{\partial t} + \frac{\partial \rho u_\alpha}{\partial x_\alpha} = 0, \quad (2.1a)$$

$$\frac{\partial \rho u_\alpha}{\partial t} + \frac{\partial \rho u_\alpha u_\beta}{\partial x_\beta} = -\frac{\partial P}{\partial x_\alpha} + \frac{\partial \tau_{\alpha\beta}}{\partial x_\beta}, \quad (2.1b)$$

where  $P$  is the pressure,  $\tau_{\alpha\beta}$  is the shear-stress tensor. The general relation between  $\tau_{\alpha\beta}$  and the shear-rate tensor  $\dot{\gamma}_{\alpha\beta}$  can be expressed as

$$\tau_{\alpha\beta} = \mu \dot{\gamma}_{\alpha\beta}, \quad (2.2)$$

where  $\mu$  is the dynamic viscosity, which can be related to the kinematic viscosity  $\nu$  by

$$\mu = \rho \nu. \quad (2.3)$$

The viscosity coefficient  $\mu$  in Eq. (2.2) is constant for the Newtonian flows, while it is a function of the local shear-rate tensor  $\dot{\gamma}_{\alpha\beta}$  for the generalized Newtonian fluids. The shear-stress tensor  $\tau_{\alpha\beta}$  for the generalized Newtonian fluids can be expressed as

$$\tau_{\alpha\beta} = \mu(|\dot{\gamma}|) \dot{\gamma}_{\alpha\beta}, \quad (2.4)$$

where  $\mu(|\dot{\gamma}|)$  is usually defined as the 'effective viscosity'.

The power-law model [4], as one of the most commonly used generalized Newtonian model, is mainly used for modeling the shear-thinning or shear-thickening behavior of non-Newtonian fluids [27–30]. The shear stress in the power-law model is defined by [4]

$$\tau_{\alpha\beta} = m |\dot{\gamma}|^{n-1} \dot{\gamma}_{\alpha\beta}, \quad n > 0, \quad (2.5)$$

where  $m$  and  $n$  are constants for a particular fluid,  $m$  is an indicator of the degree of the fluid viscosity, known as the consistent factor,  $n$  is the power-law index, and related to the degree of non-Newtonian behavior. Note that the case  $n < 1$  corresponds to the shear-thinning (pseudo-plastic) fluid, whereas  $n > 1$  corresponds to the shear-thickening (dilatant) fluid, and  $n = 1$  is the Newtonian fluid.

We denote a second invariant of the strain rate tensor as

$$D_\Pi = \sum_{\alpha, \beta} S_{\alpha\beta} S_{\alpha\beta}, \quad (2.6)$$

where  $S_{\alpha\beta}$  is the strain-rate tensor with  $\dot{\gamma} = 2S_{\alpha\beta} = 2(\nabla_{\alpha}u_{\beta} + \nabla_{\beta}u_{\alpha})$ , and

$$|\dot{\gamma}| = \sqrt{2D_{\Pi}}. \quad (2.7)$$

For a power-law fluid in the two-dimensional square cavity, the Reynolds number can be defined as [13]

$$Re = \frac{u_0^{2-n} L^n}{m}, \quad (2.8)$$

where  $u_0$  is the driven velocity on the top wall,  $L$  is the length of the cavity (see Fig. 1). Substituting Eqs. (2.7) and (2.8) into Eq. (2.5), we can obtain the effective viscosity for the power-law fluid

$$\mu_{\alpha\beta}(|\dot{\gamma}_{\alpha\beta}|) = m|\dot{\gamma}_{\alpha\beta}|^{n-1} = \frac{u_0^{2-n} L^n}{Re} (2D_{\Pi})^{\frac{n-1}{2}}. \quad (2.9)$$

### 3 Numerical method and boundary conditions

#### 3.1 Lattice Boltzmann method with MRT model

The LBM can be viewed as a finite-difference version of the continuous Boltzmann equation on a discrete lattice with a discrete set of velocity distribution functions. In the LBM, the particle distribution function  $f_i(x, t)$  denotes the particle moving with velocity  $c_i$  at time  $t$  and position  $x$ . Without loss of generalization, a two-dimensional model with nine velocities (D2Q9 model) is used in this paper. The discrete velocities in D2Q9 model are

$$\mathbf{c}_i = c\mathbf{e}_i = \begin{cases} (0,0)c, & i=0, \\ (\cos[(i-1)\pi/2], \sin[(i-1)\pi/2])c, & i=1,2,3,4, \\ 2(\cos[(i-5)\pi/2 + \pi/4], \sin[(i-5)\pi/2 + \pi/4])c, & i=5,6,7,8, \end{cases} \quad (3.1)$$

where  $c = \delta x / \delta t$  is the particle velocity,  $\delta x$  and  $\delta t$  are the lattice spacing and time step, respectively.

The MRT model can be viewed as an extension to the LBGK model. The main idea of the MRT model is that the collision is mapped onto the momentum space by multiplying a transformation matrix  $\mathbf{M}$ , whereas the streaming is still conducted in the velocity space, the evolution equation of MRT model [29] reads

$$f_i(\mathbf{x} + \mathbf{c}_i \delta t, t + \delta t) - f_i(\mathbf{x}, t) = - \sum_{j=0}^8 (\mathbf{M}^{-1} \hat{\mathbf{S}} \mathbf{M})_{ij} [f_j(\mathbf{x}, t) - f_j^{(eq)}(\mathbf{x}, t)], \quad (3.2)$$

where  $f_j^{(eq)}$  is the equilibrium distribution function, and given by

$$f_j^{(eq)} = \rho \omega_j \left[ 1 + 3 \frac{\mathbf{e}_j \cdot \mathbf{u}}{c} + 4.5 \frac{(\mathbf{e}_j \cdot \mathbf{u})^2}{c^2} - 1.5 \frac{\mathbf{u} \cdot \mathbf{u}}{c^2} \right], \quad (3.3)$$

with  $\omega_0 = 4/9$ ,  $\omega_{1-4} = 1/9$ ,  $\omega_{5-8} = 1/36$ .

If we introduce a 9-dimensional column vector  $\mathbf{f}$ ,

$$\mathbf{f}(\mathbf{x}, t) = [f_0(\mathbf{x}, t), f_1(\mathbf{x}, t), \dots, f_8(\mathbf{x}, t)]^T,$$

Eq. (3.2) can be rewritten as

$$\mathbf{f}(\mathbf{x} + \mathbf{c}\delta t, t + \delta t) - \mathbf{f}(\mathbf{x}, t) = -\mathbf{M}^{-1}\hat{\mathbf{S}}[\mathbf{m}(\mathbf{x}, t) - \mathbf{m}^{(eq)}(\mathbf{x}, t)], \quad (3.4)$$

where  $\mathbf{m} = \mathbf{M}\mathbf{f}$ ,  $\mathbf{f} = \mathbf{M}^{-1}\hat{\mathbf{m}}$ ,  $\hat{\mathbf{S}} = \mathbf{M}\mathbf{S}\mathbf{M}^{-1}$ .  $\mathbf{m}$  is a new column vector of macroscopic variables [17]

$$\mathbf{m} = \mathbf{M}\mathbf{f} = (\rho, e, \varepsilon, j_x, j_y, q_x, q_y, p_{xx}, p_{xy}), \quad (3.5)$$

where  $\rho$  and  $e$  refer to the fluid density and energy,  $j_x$  and  $j_y$  are the mass flux in two directions,  $q_x$  and  $q_y$  correspond to the energy flux in two directions,  $p_{xx}$  and  $p_{xy}$  are the diagonal and off the diagonal components of the viscous stress tensor. The transformation matrix  $\mathbf{M}$  used in the present study is given by

$$\mathbf{M} = \begin{bmatrix} 1 & 1 & 1 & 1 & 1 & 1 & 1 & 1 & 1 \\ -4 & -1 & -1 & -1 & -1 & 2 & 2 & 2 & 2 \\ 4 & -2 & -2 & -2 & -2 & 1 & 1 & 1 & 1 \\ 0 & 1 & 0 & -1 & 0 & 1 & -1 & -1 & 1 \\ 0 & -2 & 0 & 2 & 0 & 1 & -1 & -1 & 1 \\ 0 & 0 & 1 & 0 & -1 & 1 & 1 & -1 & -1 \\ 0 & 0 & -2 & 0 & 2 & 1 & 1 & -1 & -1 \\ 0 & 1 & -1 & 1 & -1 & 0 & 0 & 0 & 0 \\ 0 & 0 & 0 & 0 & 0 & 1 & -1 & 1 & -1 \end{bmatrix},$$

the collision matrix  $\hat{\mathbf{S}} = \mathbf{M}\mathbf{S}\mathbf{M}^{-1}$  in moment space is a diagonal matrix, and is given by

$$\hat{\mathbf{S}} = \text{diag}[s_0, s_1, s_2, s_3, s_4, s_5, s_6, s_7, s_8],$$

whose element represents the reciprocal of the relaxation time for the different moment term relaxing its equilibrium state. In this work, the relaxation parameters in the collision matrix  $\hat{\mathbf{S}}$  are chosen as

$$s_0 = s_3 = s_5 = 0.0, \quad s_1 = 1.1, \quad s_2 = 1.0, \quad s_4 = s_6 = 1.2, \quad s_7 = s_8 = 1/\bar{\tau}. \quad (3.6)$$

One thing should be pointed out that the different choices of the relaxation factors can make the MRT model be superior over the BGK model in stability and accuracy [26]. The relaxation rates chosen in our paper are only a special choice based on the work of Lallemand and Luo [17], and has been used in our previous work [22, 29]. In Eq. (3.6),  $\bar{\tau}$  is the relaxation time in the LBGK model and related to the dynamic viscosity  $\mu$  by

$$\mu = \rho \frac{1}{3} (\bar{\tau} - 0.5) \frac{\delta x^2}{\delta t}. \quad (3.7)$$

The local density  $\rho$  and velocity  $\mathbf{u}$  in Eq. (3.3) at each site are calculated from the distribution function

$$\rho = \sum_{j=0}^8 f_j, \quad \mathbf{u} = \frac{1}{\rho} \sum_{j=0}^8 c_j f_j. \quad (3.8)$$

We also would like to point out that the evolutionary progress of MRT model also includes two steps:

(i) Collision step in the momentum space:

$$\mathbf{m}^* = \mathbf{m} - \hat{\mathbf{S}}[\mathbf{m} - \mathbf{m}^{(eq)}], \quad (3.9a)$$

where  $*$  denotes the post-collision state, and  $\mathbf{m}^{(eq)}$  is the equilibrium distribution function in moment space.

(ii) Propagation step in velocity space:

$$f_j(\mathbf{x} + \mathbf{c}_j \delta t, t + \delta t) = f_j^*(\mathbf{x}, t), \quad \mathbf{f}^* = \mathbf{M}^{-1} \mathbf{m}^*. \quad (3.9b)$$

Finally, in the incompressible condition, the Navier-Stokes equations can be recovered from the lattice Boltzmann equation through Chapman-Enskog expansion [14]:

$$\frac{\partial \rho}{\partial t} + \frac{\partial \rho u_\alpha}{\partial x_\alpha} = 0, \quad (3.10a)$$

$$\frac{\partial \rho u_\alpha}{\partial t} + \frac{\partial \rho u_\alpha u_\beta}{\partial x_\beta} = -\frac{\partial P}{\partial x_\alpha} + \frac{\partial}{\partial x_\beta} \left[ \rho v \left( \frac{\partial u_\alpha}{\partial x_\beta} + \frac{\partial u_\beta}{\partial x_\alpha} \right) \right]. \quad (3.10b)$$

In what follows, we will present a brief discussion on how to derive the effective viscosity of power-law fluid  $\mu_{\alpha\beta}$  with MRT model. According to Eq. (2.9),  $\mu_{\alpha\beta}$  is determined by the second invariant of the strain rate tensor  $D_{\Pi}$ , so we need to derive the strain-rate tensor  $S_{\alpha\beta}$ . In LBM, the strain-rate tensor  $S_{\alpha\beta}$  can be obtained locally from the non-equilibrium parts, expressed as follows [14]

$$S_{\alpha\beta} = -\frac{3}{2\rho\tau\delta t} \sum_{j=0}^8 c_{j\alpha} c_{j\beta} [f_j(\mathbf{x}, t) - f_j^{eq}(\mathbf{x}, t)], \quad (3.11)$$

while the formula of  $S_{\alpha\beta}$  in MRT-LB is more complex with the following form [29]:

$$S_{\alpha\beta} = -\frac{3}{2\rho\delta t} \sum_{i=0}^8 c_{i\alpha} c_{i\beta} \sum_{j=0}^8 (\mathbf{M}^{-1} \hat{\mathbf{S}} \mathbf{M})_{ij} [f_j(\mathbf{x}, t) - f_j^{eq}(\mathbf{x}, t)]. \quad (3.12)$$

Then, substituting Eqs. (2.6) and (2.7) into (2.9) with the term  $S_{\alpha\beta}$  given by Eq. (3.12), and for a specific fluid with a given  $Re$  and  $n$ , one can obtain the effective viscosity  $\mu_{\alpha\beta}$  according to Eq. (2.9). And simultaneously, the relaxation parameter  $s_8$  is derived via Eq. (3.7), which is used to perform the collision step. It is noted that in the simulation

of the non-Newtonian fluid flows, the effective viscosity and relaxation parameters are functions of space and time, which should be updated in each iterate step.

The numerical procedure of present non-Newtonian MRT model is summarized as follows:

- (i) Initialize all the values of the density and velocity based on the physical problem, then the equilibrium distribution function  $f_j^{eq}$  can be determined from Eq. (3.3), which is used to initialize the distribution function  $f_j$ .
- (ii) Calculate the effective viscosity  $\mu$  based on Eqs. (2.6)-(2.9) and (3.12) (Details can be found in the above analysis). Once the effective viscosity are known, we can derive the local  $\bar{\tau}$  from Eq. (3.7).
- (iii) Execute the collision and propagation steps based on Eqs. (3.9), and compute the macroscopic quantities from Eq. (3.8).
- (iv) Go to step (ii) and update  $\bar{\tau}$  and  $f_j$ .

The process runs until the following convergent criterion is satisfied:

$$|u(x_c, y_c, t+100) - u(x_c, y_c, t)| < 1.0e-9. \quad (3.13)$$

### 3.2 Boundary conditions

The implementation of the boundary conditions is also a crucial issue since it has an important influence on the accuracy and stability of the LBM. The distribution function  $f_i(\mathbf{x}, t)$  is usually not given directly at the boundaries. Therefore, we must determine the distribution function at the boundaries from the given macroscopic variables. In the present work, treatments for the boundary conditions on the solid walls using the non-equilibrium extrapolations scheme proposed by Guo et al. [31] for its second-order in numerical accuracy. According to the scheme, the distribution function  $f_i(\mathbf{x}, t)$  at the boundary can be decomposed into its equilibrium and non-equilibrium parts. When compute the distribution function of boundary node  $\mathbf{x}_b$ , taking velocity of boundary node and the nearest fluid node  $\mathbf{x}_f$  to compute the equilibrium and the non-equilibrium parts, respectively. Therefore we can derive all the unknown distribution functions at the boundary from the followed equation:

$$f_i(\mathbf{x}_b, t) = f_i^{eq}(\mathbf{x}_b, t) + f_i(\mathbf{x}_f, t) - f_i^{eq}(\mathbf{x}_f, t). \quad (3.14)$$

## 4 Numerical simulations and discussions

### 4.1 Lid-driven cavity flow

The schematic of a lid-driven cavity is shown in Fig. 1, where the upper lid is moving from left to right with a constant velocity  $u_0=0.1$ , whereas the other three walls are fixed, the length  $L=1.0$ . In our simulations, the nodes on the top corners belong to the moving lid with the constant velocity  $u_0$ , and the bottom corners belong to wall with zero velocity,

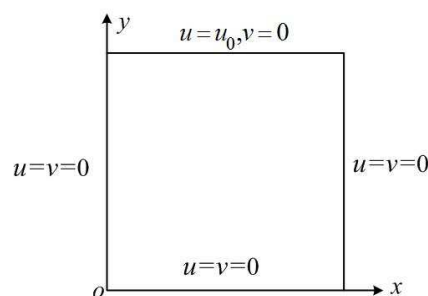


Figure 1: Geometry and boundary conditions of the lid-driven cavity.

and then non-equilibrium extrapolations scheme introduced above is implemented in the boundary treatment. In the following parts, we first validate MRT model through a comparison with some available results, followed by studies of grid-independence and Mach number ( $Ma$ ) effects. Then we will further investigate the complex characteristics of the power-law fluid flows in the lid-driven cavity for different Reynolds number ( $Re$ ) and power-law index ( $n$ ).

## 4.2 Validation of the MRT model

We first performed some simulations for Newtonian and non-Newtonian fluid flows ( $n=1.0, 0.5$  and  $1.5$ ), and show numerical results in Figs. 2 and 3. As shown in these figures, the present results are in good agreement with some previous results [3, 4, 18]. Then, we also compare the central location ( $x_c, y_c$ ) and stream function value ( $\phi_c$ ) of the primary vortex with some published results [3, 4] in Tables 1 and 2. From these tables, we find the

Table 1: Comparison of present simulations for Newtonian fluid and non-Newtonian fluid flows ( $Re=100, 500$ ).

Location of vortex		$n=0.50$	$n=0.75$	$n=1.00$	$n=1.50$
$x_c$ ( $Re=100$ )	Neofytou [4]	0.7166	0.6577	0.6123	0.5647
	Present results	0.7168	0.6576	0.6166	0.5628
$y_c$ ( $Re=100$ )	Neofytou [4]	0.7804	0.7478	0.7359	0.7240
	Present results	0.7826	0.7498	0.7379	0.7282
$x_c$ ( $Re=500$ )	Neofytou [4]	0.5731	—	0.5494	0.5495
	Present results	0.5793	—	0.5467	0.5495
$y_c$ ( $Re=500$ )	Neofytou [4]	0.5490	—	0.5935	0.6380
	Present results	0.5497	—	0.5947	0.6378

Table 2: Comparison of present simulations for Newtonian fluid and non-Newtonian fluid flows ( $Re=100$ ).

The value of the stream function		$n=0.25$	$n=1.00$	$n=1.50$
$\phi_c$ ( $Re=100$ )	Bell & Surana [3]	-0.298	-0.103	-0.117
	Present results	-0.2953	-0.1023	-0.1152

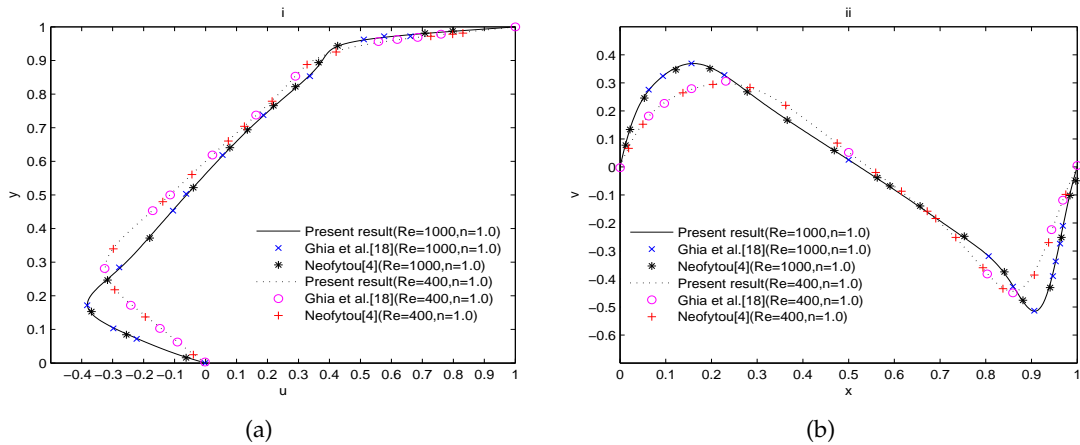


Figure 2: Comparison between present results and previous result [4, 18] for Newtonian flows: (a)  $u$ -velocity profiles along the vertical centerline of the cavity. (b)  $v$ -velocity profiles along the horizontal centerline of the cavity.

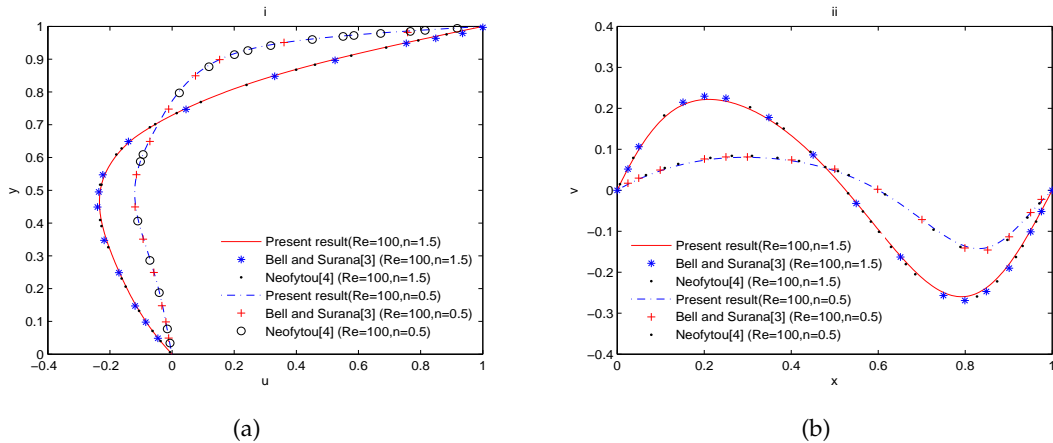


Figure 3: Comparison between present results and previous results [3, 4] for non-Newtonian flows: (a)  $u$ -velocity profiles along the vertical centerline of the cavity; (b)  $v$ -velocity profiles along the horizontal centerline of the cavity.

results obtained with MRT model agree well with some previous works. Besides, we also made a comparison between results from BGK model and MRT model for simulating non-Newtonian flows in a driven cavity. For BGK model, the maximum of  $Re$  that can be tested in our study is only about 22000 for case  $n = 1.75$  and 20000 for case  $n = 0.25$ . However, for MRT model, the maximum of  $Re$  can reach to 100000 and beyond.

Before we proceed any further, it is essential to guarantee that the results are grid-independent and the compressible effects are negligible. For the former purpose, we carried out some simulations on two different uniform grids namely  $256 \times 256$ ,  $512 \times 512$  for the non-Newtonian fluid flows with  $Re=10000$ . The results are shown in Fig. 4 (a) for

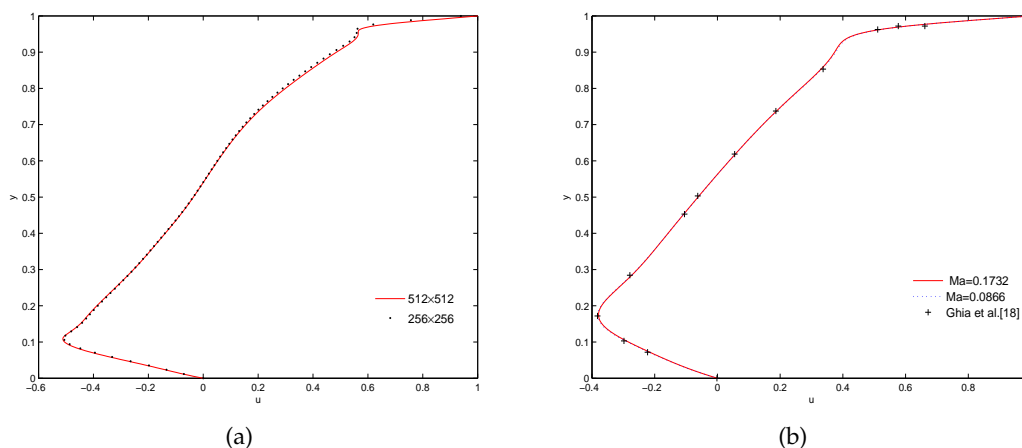


Figure 4: (a)  $u$ -velocity profiles along the vertical centreline of the cavity for two grids (non-Newtonian flow,  $Re = 10000$ ). (b)  $u$ -velocity profiles along the vertical centreline of the cavity for two  $Ma$  (Newtonian flow  $Re = 1000$ ) as well as comparison with previous results [18].

the  $u$ -velocity profiles along the vertical centerline of the cavity. It can be seen that the grid number  $256 \times 256$  is fine enough to derive grid-independent results, and therefore this grid is also used for all subsequent computations. For the latter purpose, we carried out a comparison study of two sets of  $Ma$  number:  $Ma_1 = 0.1732$  (corresponding to  $u = 0.1$  which is involved in our later study) and  $Ma_2 = 0.0866$  (corresponding to  $u = 0.05$ ) with a fixed  $Re = 1000$ . We present  $u$ -velocities along the vertical centerline in Fig. 4 (b), and find that the Mach number has a negligible effect.

Through above numerical results, one can find that the MRT model indeed has a strong capacity in studying problem of power-law fluids in the lid-driven cavity, and especially in simulating high Reynolds number problems.

### 4.3 The effects of the Reynolds number on power-law fluid flows in the lid-driven cavity

In this section, particularly but without loss of generality, we mainly consider the simulation for the power-law index  $n = 1.5$  which shows the 'dilatant' or 'shear-thickening' behavior of the fluids and  $n = 0.5$  which indicates the behavior of 'pseudo-plastic' or 'shear-thinning'.

We first carried out a large number of simulations for shear-thickening flows ( $n = 1.5$ ), and showed the streamlines in Fig. 5 and variations of primary vortex location in Fig. 6, where  $Re$  is ranged from 100 to 10000. As seen from Fig. 5, the Reynolds number has great effects on the flow structure. When  $Re$  is less than 3000, only three vortices appear in the cavity, a primary one in the center and a pair of secondary ones in the lower corners of the cavity. With the increase of  $Re$ , the primary vortex, generated by the motion of the upper lid, gradually deviates the top right corner, and moves towards the center of the

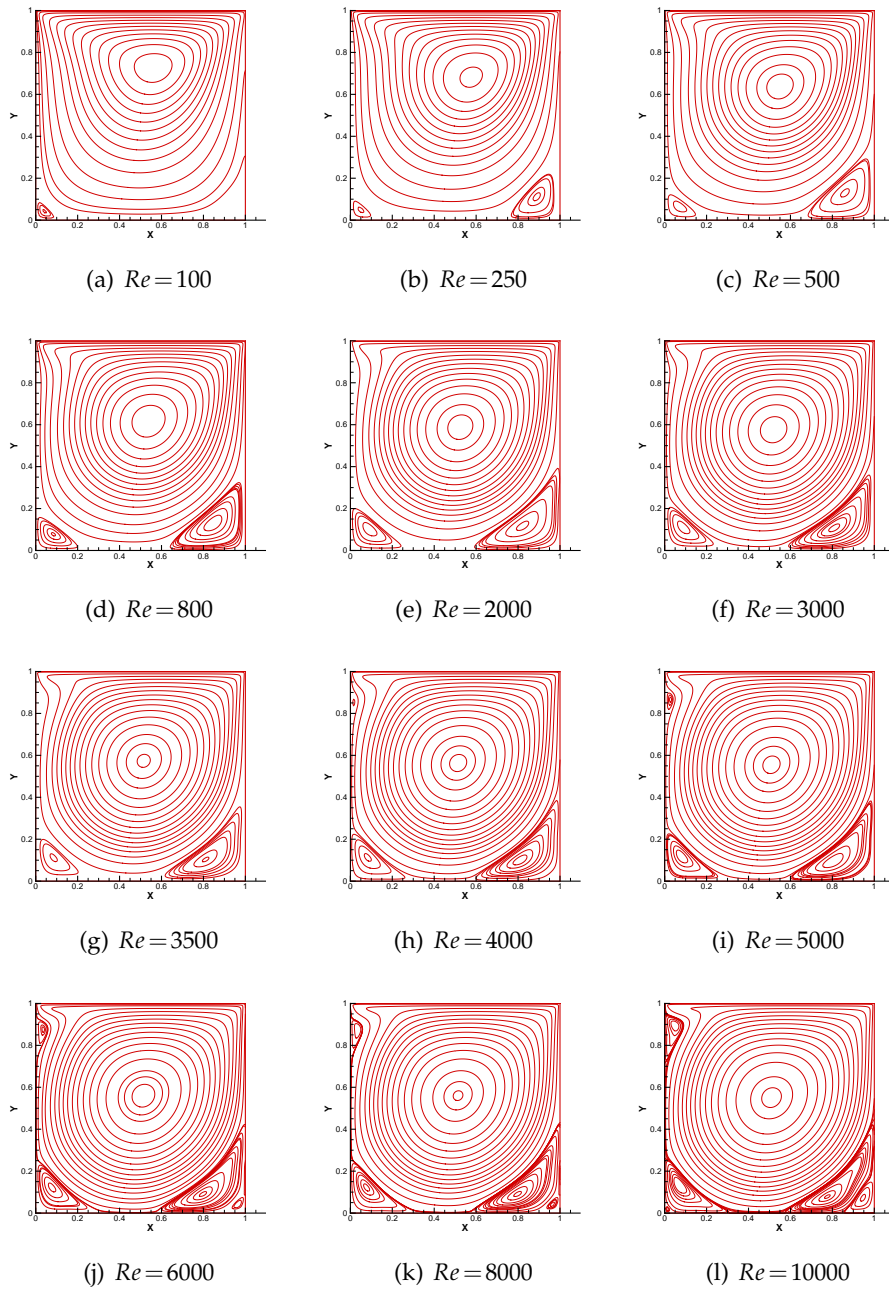


Figure 5: Streamlines of shear-thickening flow ( $n=1.5$ ) for different  $Re$ .

cavity (Fig. 6). However, when  $Re$  is increased to 4000, a third secondary vortex is found near the top left corner; when  $Re$  is further increased to 6000, a tertiary vortex appears in the bottom right corner.

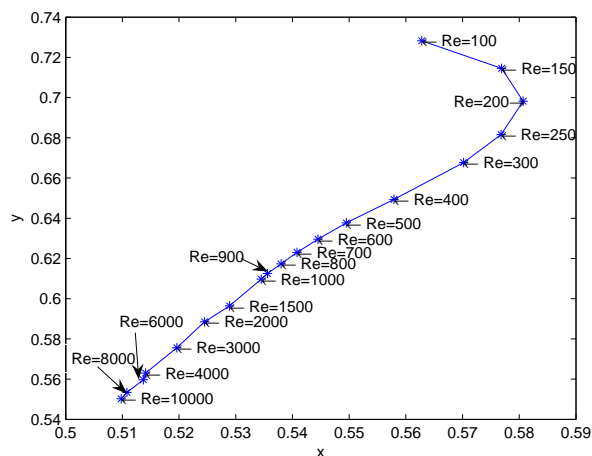


Figure 6: Effects of Reynolds number on location of primary vortex centers for the case  $n = 1.5$ .

Additionally, we present the  $x$ -,  $y$ -coordinates and stream function value of the primary and secondary vortices that successively appear in the lower right and left corners of the cavity in Table 3. In Table 3, the letters  $x$ ,  $y$  denote the  $x$ -,  $y$ -coordinates and stream

Table 3: Stream function values and positions of the primary and second vortices for different  $Re$  ( $n = 1.5$ ).

$Re$	$x_c$	$y_c$	$\phi_c$	$x_r$	$y_r$	$\phi_r$	$x_l$	$y_l$	$\phi_l$
100	0.5628	0.7282	-0.11522	0.9300	0.0658	-1.3467e-5	0.0425	0.0423	1.577e-5
150	0.5769	0.7145	-0.11767	0.9179	0.0895	6.7255e-5	0.0426	0.0457	1.7e-5
200	0.5807	0.6982	-0.11985	0.9019	0.1077	0.0002261	0.0447	0.0484	2.061e-5
250	0.5768	0.6816	-0.12203	0.8923	0.1174	0.0004338	0.0496	0.0498	2.8e-5
300	0.5702	0.6677	-0.12377	0.8830	0.1238	0.0006575	0.0539	0.0527	3.741e-5
400	0.5579	0.6494	-0.1264	0.8696	0.1295	0.0010865	0.0631	0.0581	6.0e-5
500	0.5495	0.6377	-0.1284	0.8613	0.1314	0.0014551	0.0708	0.0646	0.00010
600	0.5445	0.6296	-0.1299	0.8552	0.1315	0.0017689	0.0770	0.0697	0.00015
700	0.5408	0.6230	-0.1310	0.8507	0.1308	0.002034	0.0810	0.0741	0.00020
800	0.5380	0.6173	-0.1320	0.8471	0.1297	0.002262	0.0839	0.0779	0.00025
900	0.5356	0.6125	-0.1329	0.8441	0.1287	0.002458	0.0858	0.0812	0.00030
1000	0.5345	0.6097	-0.1336	0.8404	0.1285	0.002593	0.0872	0.0844	0.00033
1500	0.5289	0.5964	-0.1364	0.8294	0.1227	0.003142	0.0902	0.0951	0.00051
2000	0.5245	0.5885	-0.13837	0.8216	0.1163	0.003503	0.0905	0.1009	0.00066
3000	0.5196	0.5756	-0.14077	0.8096	0.1080	0.003721	0.0875	0.1110	0.00081
3500	0.5151	0.5737	-0.14177	0.8106	0.1031	0.003973	0.0845	0.11205	0.00104
4000	0.5141	0.5630	-0.14029	0.8098	0.0997	0.004133	0.0821	0.1135	0.00119
5000	0.5133	0.5614	-0.13802	0.8040	0.0949	0.004252	0.0792	0.1183	0.00131
6000	0.5137	0.5597	-0.1382	0.7982	0.0909	0.004320	0.0765	0.1227	0.00140
8000	0.5108	0.5534	-0.13657	0.7873	0.0843	0.004294	0.0728	0.1284	0.00152
10000	0.5098	0.5502	-0.13511	0.7763	0.0787	0.004211	0.0698	0.1332	0.00159

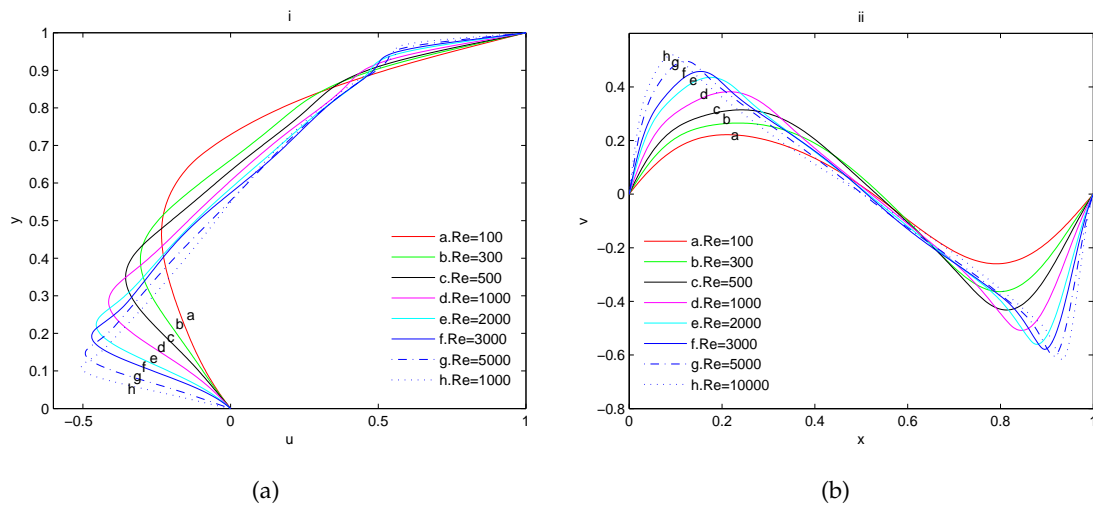


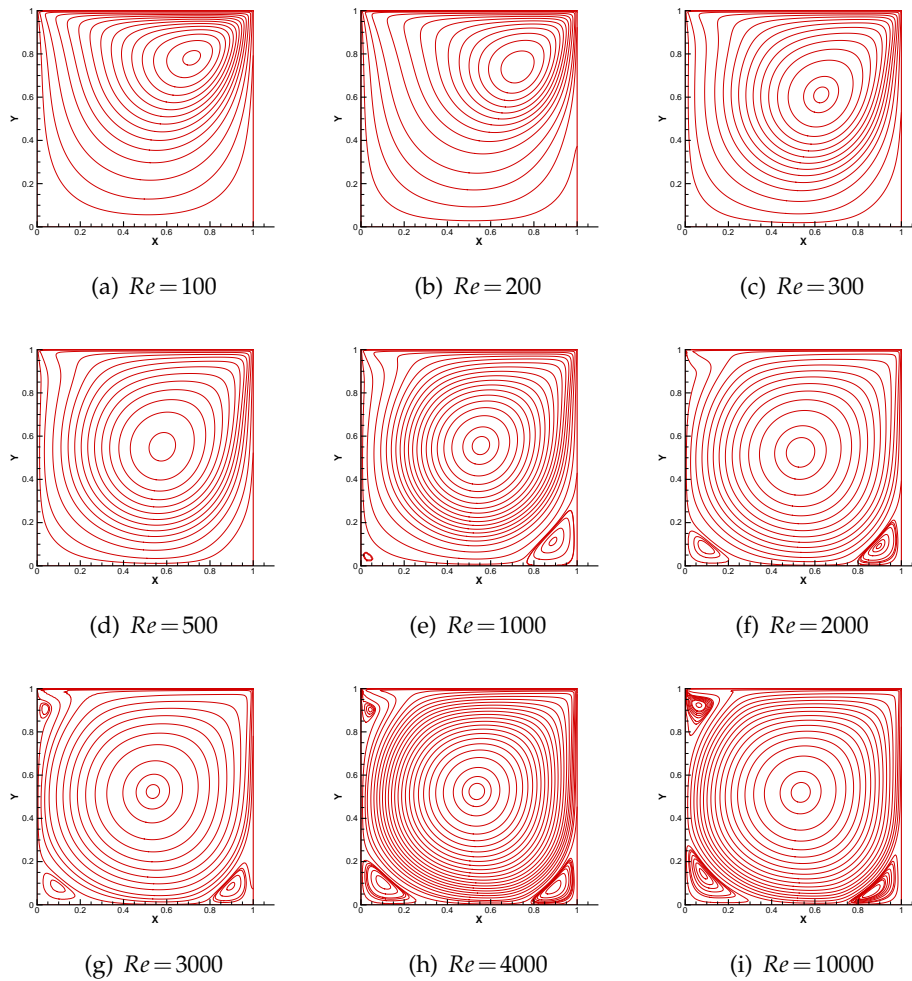
Figure 7: Effects of Reynolds number on the velocity profiles for the case  $n = 1.5$ . (a)  $u$ -velocity profiles along the vertical centerline of the cavity; (b)  $v$ -velocity profiles along the horizontal centerline of the cavity.

function value of the vortex; the subscript denotes the vortex location. (For example,  $c$  refers to the primary vortex at the center of the cavity,  $r$  and  $l$  refer to the secondary vortices in the lower right and left). The results show that, firstly, the stream function value of the primary vortex keeps increasing when  $Re$  is less than 3500, but an opposite tendency is observed for  $Re > 3500$ ; Secondly, the variation of strength of the secondary vortex near bottom right corner is similar to that of the primary vortex, whereas the strength of another second vortex increases with the increase of the Reynolds number.

To see the effects of the Reynolds number clearly, the variation of velocity profiles at centerlines with  $Re$  is also shown in Fig. 7. As seen from Fig. 7, the Reynolds number also has great effects on the velocity profiles. The  $u$ -velocity profiles along the vertical centerline and  $v$ -velocity profiles along the horizontal centerline of the cavity exhibit a more dramatic change for higher  $Re$ . With the increase of  $Re$ , the velocity profiles in the centerline of the cavity approach linearly, which means the uniform vortex region is generated in the cavity core at higher values of  $Re$ . In short, the increase of  $Re$  not only leads the number of vortex to increase, but also brings more complex flow structures.

On the other hand, we also performed a lot of numerical simulations for the shear-thinning fluid flows ( $n=0.5$ ), and presented the results in Fig. 8 and Table 4. As seen from Fig. 8, the flow structure of the case  $n=0.5$  is similar to that of the case  $n=1.5$ . However, for the case  $n=0.5$ , the stream function value of the primary vortex keeps decreasing with the increase of  $Re$ , which are different from the phenomena observed for the case  $n=1.5$ .

In conclusion, although the flow structure of power-law fluids (shear-thickening or shear-thinning) is very similar to those of the Newtonian fluids, the strengths of them are different with each other for a fixed  $Re$ .

Figure 8: Streamlines of shear-thinning flow ( $n=0.5$ ) for different  $Re$ .Table 4: Stream function values and positions of the primary and second vortices for different  $Re$  ( $n=0.5$ ).

$Re$	$x_c$	$y_c$	$\phi_c$	$x_r$	$y_r$	$\phi_r$	$x_l$	$y_l$	$\phi_l$
100	0.7168	0.7826	-0.0648	—	—	—	—	—	—
200	0.6647	0.6699	-0.0638	—	—	—	—	—	—
300	0.6224	0.6013	-0.0623	—	—	—	—	—	—
500	0.5793	0.5497	-0.0611	—	—	—	—	—	—
1000	0.5468	0.5280	-0.0597	—	—	—	—	—	—
2000	0.5338	0.5245	-0.0583	0.8976	0.0939	0.00035	0.0947	0.0877	7.2e-005
3000	0.5365	0.5180	-0.0485	0.8945	0.0857	0.00041	0.0996	0.0957	0.00011
4000	0.5359	0.5235	-0.0440	0.8919	0.0802	0.00044	0.1011	0.1040	0.00017
5000	0.5255	0.5190	-0.0477	0.8683	0.0768	0.0006	0.0945	0.1206	0.00033
10000	0.5347	0.5183	-0.0330	0.8595	0.0588	0.00056	0.0820	0.1446	0.00039

#### 4.4 The effects of power-law index on power-law fluid flows in the lid-driven cavity

In this section, we will investigate the effects of power-law index on the flow structure. To this end, the Reynolds number  $Re$  is first fixed, the power-law index  $n$  is changed from 0.25 to 1.75, which covers the shear-thinning, Newtonian and shear-thickening fluids. The numerical results of  $Re=100$  and 500 under different power-law index are presented in Figs. 9-13. (For case  $Re=100$  and  $n=1.75$ , the simulation results are divergent.)

The effects of the power-law index on fluid structure are shown in Figs. 9 and 10. From these figures, it is found that the flow structure are very similar to each other for a fixed Reynolds number, with the increase of the power-law index, the number of vortex appeared in the cavity increases, and more complex flow phenomena are also observed. The effects of the power-law index  $n$  on the  $u$  and  $v$  profiles along the vertical and horizontal centerlines are shown in Fig. 11 ( $Re=100$ ) and Fig. 12 ( $Re=500$ ), respectively. As seen from Figs. 11 (a), the increase of  $n$  leads the velocity to increase near the top and bottom of the cavity. In Fig. 11 (b), the configuration of  $v$ -velocity appears a sinusoidal profile, and becomes sharper with an increase of  $n$ , the peak value of the  $v$ -velocity along the horizontal centerline also increases in  $n$ . These observations are attributed to the gradual decrease (shear-thinning case) or increase (shear-thickening case) of the viscous effects with the increase of  $n$ . Compared to the velocity profiles presented in Fig. 10, the

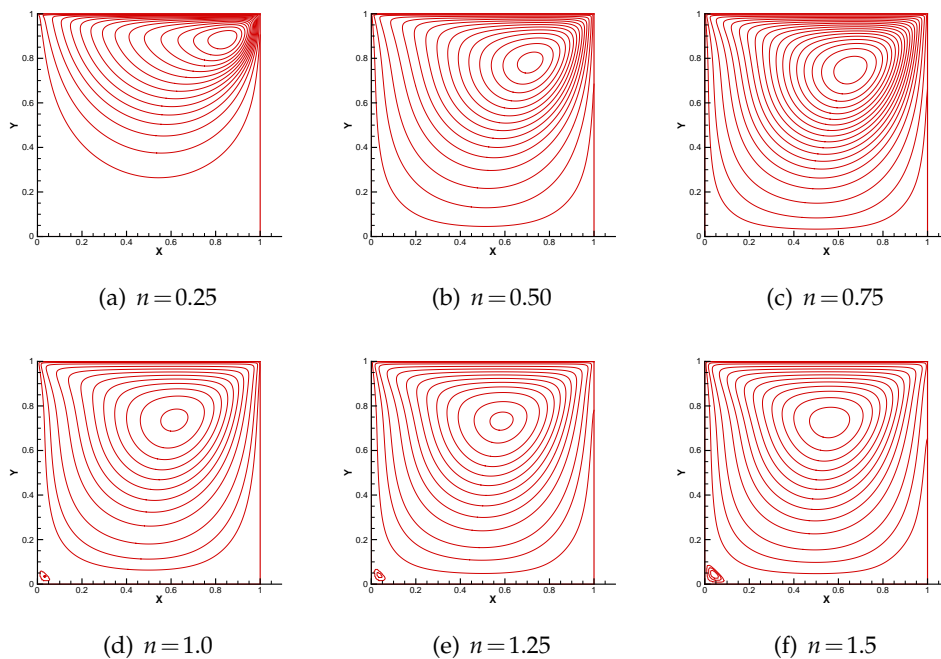


Figure 9: Streamlines of flow ( $Re=100$ ) for different  $n$ .

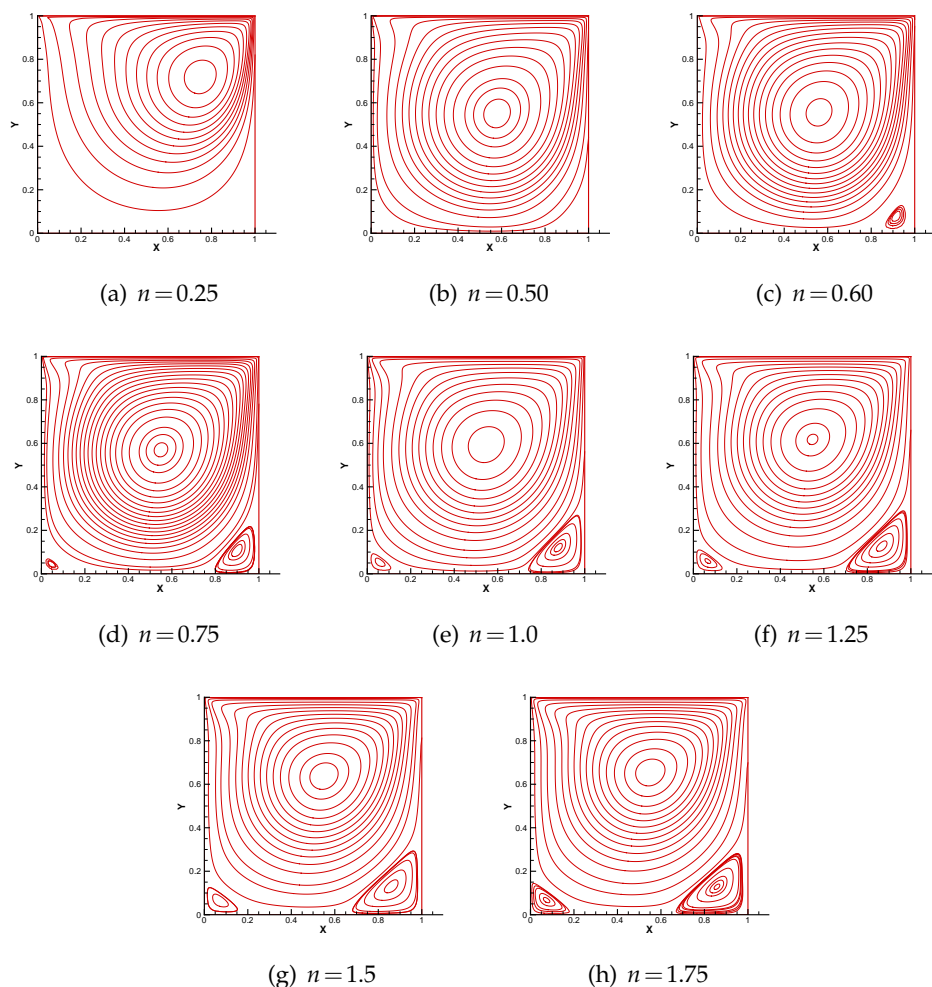


Figure 10: Streamlines of flow ( $Re = 500$ ) for different  $n$ .

velocity distributions for case  $Re = 500$  show in Fig. 12 seem to be similar to the case  $Re = 100$ , however, the amplitude of the velocity vibration is much larger than that of the case  $Re = 100$ , which is caused by the larger inertial effect of a higher  $Re$ . In addition, the effects of power-law index on location and stream function value of primary vortex are also studied, the corresponding results are shown in Fig. 13. For the case  $Re = 100$ , we can see from Fig. 13 (a), the primary vortex always moves from the top right corner towards the central zone with the increase of  $n$ , whereas for the case  $Re = 500$ , the primary vortex first moves towards the center of the cavity, then moves upward with the increase of  $n$ . The results in Fig. 13 (b) show that the stream function value of the primary vortex, for both cases of  $Re = 100$  and  $Re = 500$ , increase with the increase of the power-law index.

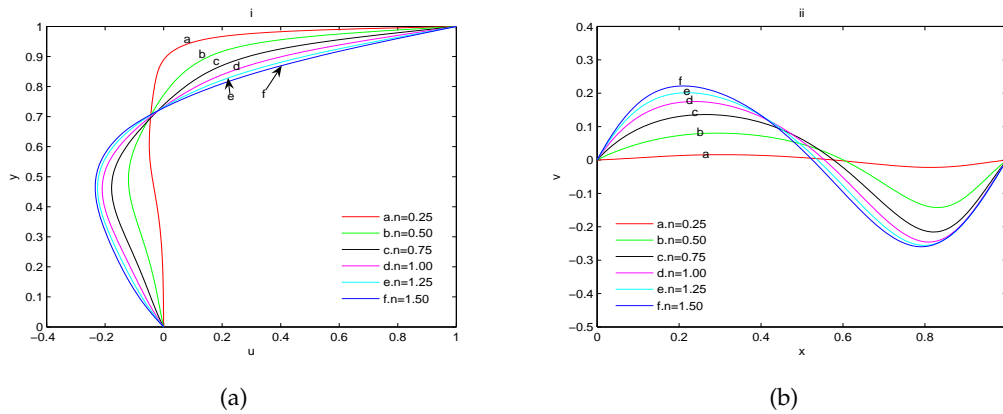


Figure 11: Effects of power-law index on the velocity profiles for power-Law fluid flows for  $Re=100$ . (a)  $u$ -velocity profiles along the vertical centerline of the cavity; (b)  $v$ -velocity profiles along the horizontal centerline of the cavity.

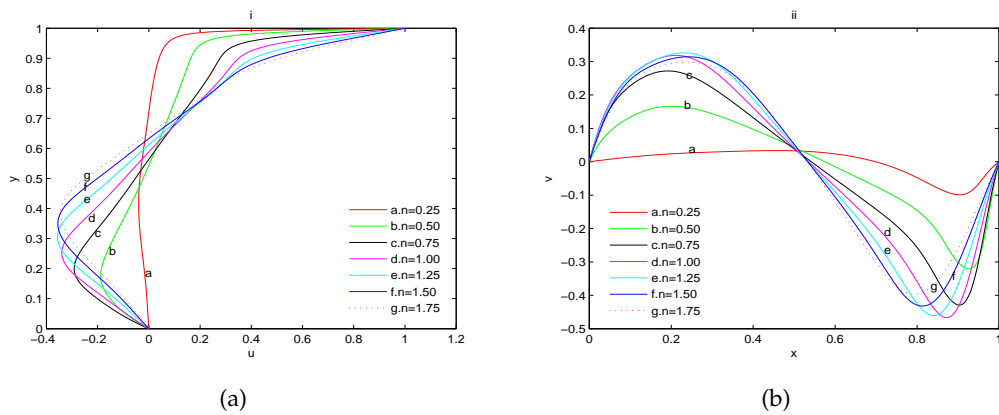


Figure 12: Effects of power-law index on the velocity profiles for power-Law fluid flows for  $Re=500$ . (a)  $u$ -velocity profiles along the vertical centerline of the cavity; (b)  $v$ -velocity profiles along the horizontal centerline of the cavity.

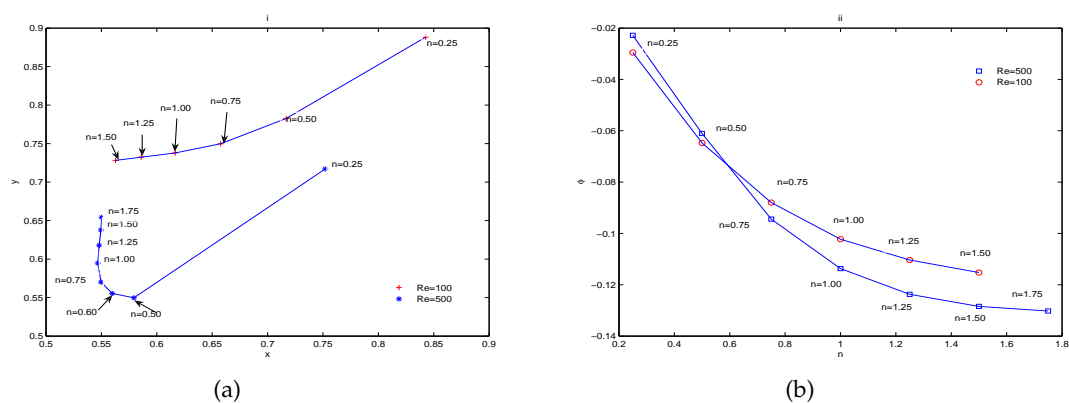


Figure 13: Effects of power-law index on location of (a) primary vortex and (b) values of stream function.

## 5 Conclusions

In this paper, the power-law fluid flow in the two-dimensional square cavity is studied by MRT-LBM. We present the complex phenomena of non-Newtonian fluid flows, the Reynolds number and non-Newtonian effects on the lid-driven cavity flows, and a detailed comparison between Newtonian and non-Newtonian fluids. Based on present numerical results, some conclusions are derived:

(1) For a fixed power-law index near unit, the flow structures of power-law fluids are similar to those of Newtonian fluid, but for other cases, there is a noticeable difference between the flow structure of power-law fluid and that of Newtonian fluid.

(2) For a fixed Reynolds number, the power-law index gives a great influence on flow structure of power-law fluids, the number and the strength of vortex appeared in the cavity.

(3) Numerical results also show that MRT model is robust when it is used to simulate non-Newtonian flows at high Reynolds number, this study can provide a reliable scientific basis in studying three dimensional non-Newtonian flows for later research.

## Acknowledgments

The authors would like to thank Prof. Nanzhong He, Dr. Jianhua Lu and Dr. Fumei Rong for many helpful suggestions and discussions during the research. This study is supported by the National Natural Science Foundation of China (Grant Nos. 11272132, 51125024, 51006040), and China Postdoctoral Science Foundation (Grant No. 2012M521424).

## References

- [1] J. R. A. Pearson, P. M. J. Tardy, Models of non-Newtonian and complex fluids through porous media, *J. Non-Newton. Fluid Mech.*, 102 (2002), 447-473.
- [2] S. P. Sullivan, L. F. Gladden, M. L. Johns, Simulation of power-law fluid flow through porous media using lattice Boltzmann techniques, *J. Non-Newton. Fluid Mech.*, 133 (2006), 91-98.
- [3] B. C. Bell, K. S. Surana, P-version least squares finite element formulation for two dimensional, incompressible, non-Newtonian, isothermal and non-isothermal flow, *Int. J. Numer. Meth. Fluids*, 18 (1994), 127-162.
- [4] P. Neofytou, A 3rd order upwind finite volume method for generalized Newtonian fluid flows, *Adv. Eng. Softw.*, 36 (2005), 664-680.
- [5] E. Aharonov, D. H. Rothman, Non-Newtonian flow through porous media: a lattice-Boltzmann method, *Geophys. Res. Lett.*, 20 (1993), 679-682.
- [6] A. Rafiee, Modelling of generalized Newtonian lid-driven cavity flow using an SPH method, *Anziam. J.*, 49 (2008), 411-422.
- [7] C. S. Huang, Z. H. Chai, and B. C. Shi, Non-Newtonian effect on hemodynamic characteristics of blood flow in stented cerebral aneurysm, *Commun. Comput. Phys.*, 13 (2013), 916-928.

- [8] R. Benzi, S. Succi, M. Vergassola, The lattice Boltzmann equation: theory and applications, *Phys. Rep.*, 222 (1992), 145-197.
- [9] C. K. Aidun and J. R. Clausen, Lattice-Boltzmann Method for Complex Flows, *Annu. Rev. Fluid Mech.*, 42 (2010), 439-472.
- [10] X. W. Shan, H. D. Chen, Lattice Boltzmann model for simulating flows with multiple phases and components, *Phys. Rev. E*, 47 (1993), 1815-1819.
- [11] S. Ubertini, S. Succi, Recent advances of Lattice Boltzmann techniques on unstructured grids, *Prog. Comput. Fluid Dyn.*, 5 (2005), 85-96.
- [12] M. Yoshino, Y. Hotta, T. Hirozane, M. Endo, A numerical method for incompressible non-Newtonian fluid flows based on the lattice Boltzmann method, *J. Non-Newt. Fluid Mech.*, 147 (2007), 69-78.
- [13] J. Boyd, J. Buick, S. Green, A second-order accurate lattice Boltzmann non-Newtonian flow model, *J. Phy. A: Math. Gen.*, 39 (2006), 14241-14247.
- [14] S. Y. Chen, G. D. Doolen, Lattice Boltzmann method for fluid flows, *Annu. Rev. Fluid Mech.*, 30 (1998), 329-364.
- [15] Y. H. Qian, D. d'Humières, P. Lallemand, Lattice BGK models for Navier-Stokes equation, *Euophys. Lett.*, 17 (1992), 479-484.
- [16] D. d'Humières, Generalized lattice Boltzmann equation, in: *Rarefied Gas Dynamics: Theory and Simulations*, Progress in Astronautics and Aeronautics, AIAA Press, Washington, DC, 159 (1992), 450-458.
- [17] P. Lallemand, L. S. Luo, Theory of the lattice Boltzmann method: Dispersion, dissipation, isotropy, and stability, *Phys. Rev. E*, 61 (2000), 6546-6562.
- [18] U. Ghia, K. N. Ghia, C. T. Shin, High-Re solutions for incompressible flow using the Navier-Stokes equations and a multigrid method, *J. Comput. Phys.*, 48 (1982), 387-411.
- [19] S. Hou, Q. Zou, S. Y. Chen, G. D. Doolen, A. C. Cogley, Simulation of cavity flow by the lattice Boltzmann method, *J. Comput. Phys.*, 118 (1995), 329-347.
- [20] P. Shankar and M. Deshpande, Fluid mechanics in the driven cavity, *Annu. Rev. Fluid Mech.*, 32 (2000), 93-136.
- [21] J. S. Wu, Y. L. Shao, Simulation of lid-driven cavity flows by parallel lattice Boltzmann method using multi-relaxation-time scheme, *Int. J. Numer. Meth. Fluids*, 46 (2004), 921-937.
- [22] Z. H. Chai, B. C. Shi, L. Zheng, Simulating high Reynolds number flow in two-dimensional lid-driven cavity by multi-relaxation-time lattice Boltzmann method, *Chin. Phys.*, 15 (2006), 1855-1864.
- [23] X. Y. Zhou, B. C. Shi, N. C. Wang, Numerical simulation of LBGK model for high Reynolds number flow, *Chin. Phys.*, 13 (2004), 712-720.
- [24] N. Z. He, N. C. Wang, B. C. Shi, Z. L. Guo, A unified incompressible lattice BGK model and its application to three-dimensional lid-driven cavity flow, *Chin. Phys.*, 13 (2004), 40-47.
- [25] T. Zhang, B. C. Shi, Z. H. Chai, Lattice Boltzmann simulation of lid-driven flow in trapezoidal cavities, *Comput. Fluids*, 39 (2010), 1977-1989.
- [26] L. S. Luo, W. Liao, X. W. Chen, Y. Peng, and W. Zhang, Numerics of the lattice Boltzmann method: Effects of collision models on the lattice Boltzmann simulations, *Phys. Rev. E*, 83 (2011), 056710.
- [27] S. Gabbanelli, G. Drazer, J. Koplik, Lattice Boltzmann method for non-Newtonian (power-law) fluids, *Phys. Rev. E*, 72 (2005), 046312.
- [28] O. Malaspinas, G. Courbebaisse, M. Deville, Simulation of generalized Newtonian fluids with the lattice Boltzmann method, *Int. J. Mod. Phys. C*, 18 (2007), 1939-1949.
- [29] Z. H. Chai, B. C. Shi, Z. L. Guo, F. M. Rong, Multiple-relaxation-time lattice Boltzmann

- model for generalized Newtonian fluid flows, *J. Non-Newton. Fluid Mech.*, 166 (2011), 332-342.
- [30] G. H. Tang, S. B. Wang, P. X. Ye, W. Q. Tao, Bingham fluid simulation with the incompressible lattice Boltzmann model, *J. Non-Newton. Fluid Mech.*, 166 (2011), 145-151.
- [31] Z. L. Guo, C. G. Zheng, B. C. Shi, Non-equilibrium extrapolation method for velocity and pressure boundary conditions in the lattice Boltzmann method, *Chin. Phys.*, 11 (2002), 366-374.